Polytopic Lyapunov Function-Based Hybrid Switching Control Strategy for High Voltage Direct Current Networks

Kamat Tarcar, Rohan; Popov, Marjan; Lekic, Aleksandra

DOI
10.1109/OAJPE.2025.3585425

Publication date
2025

Document Version
Final published version

Published in
IEEE Open Access Journal of Power and Energy

IEEE Open Access Journal of Power and Energy

Received 17 January 2025; revised 25 April 2025 and 11 June 2025; accepted 27 June 2025.
Date of publication 2 July 2025; date of current version 9 July 2025.

Digital Object Identifier 10.1109/OAJPE.2025.3585425

Polytopic Lyapunov Function-Based Hybrid Switching Control Strategy for High Voltage Direct Current Networks

ROHAN KAMAT TARCAR (Graduate Student Member, IEEE), MARJAN POPOV (Fellow, IEEE), AND ALEKSANDRA LEKIĆ (Senior Member, IEEE)

Faculty of EEMCS, Delft University of Technology, 2628 CD Delft, The Netherlands

CORRESPONDING AUTHOR: R. KAMAT TARCAR (r.kamattarcar@tudelft.nl)

ABSTRACT The increased use of High-Voltage Direct Current transmission networks requires appropriate control strategies for the converter stations, which are crucial to ensure uninterrupted energy supply. In this paper, a Polytopic Lyapunov Function-based Hybrid switching control strategy is implemented to combine the merits of Grid Following and Grid Forming control strategies by switching alternatively from one to another at the polytopes' hyperplanes to ensure good system response even for faulty conditions. The state space equations of the control strategies are used to form the state hyperplanes for the switching rule. Since the hybrid switching control is based on the Polytopic Lyapunov Function, the system is inherently Large Signal Stable. The results obtained by real-time-based simulations using RTDS verify the designed control for various transient phenomena.

INDEX TERMS Lyapunov function, modular multilevel converter, HVdc transmission system, switching control, polytopic control, grid forming control, grid following control.

I. INTRODUCTION

THE increase in electrical energy consumption and global warming has led to a global transition to greener energy alternatives such as wind and solar energy. However, these alternatives are often located in remote geographic locations [1]. The transport of vast amounts of electric power from these locations is done by using High Voltage Direct Current (HVdc) systems [2], [3]. Power electronic converters such as Modular Multilevel Converters (MMCs) that are a part of the HVdc transmission system require control strategies to regulate the power flow and maintain the DC voltage of the HVdc system [1]. The Grid Following (GFL) control strategy is mainly used because of its robust nature. Recent advances in control strategies have led to a new type of control strategy that can be applied to control converters in the HVdc systems, known as a Grid Forming (GFM) control strategy. The GFM control strategies establish stable AC voltage and frequency references for the HVdc grid, which are crucial for the synchronization of AC and DC systems [4]. GFM control strategies are ideal when the strength of the AC grid connected to the HVdc network is weak. System strength of electrical grids refers to the ability of the power system to maintain and control voltage levels at a specific location, both during normal operation and during disturbances such as faults or outages [5]. It is proportional to the fault current level at that location and inversely proportional to the effective grid impedance seen from the point of common coupling (PCC). System strength is crucial for ensuring the stability and reliability of the power system, especially as more renewable energy sources are integrated into the grid, replacing traditional synchronous fossil fuel power stations with asynchronous wind and solar farms [6].

GFL converters depend on the grid's stability and strength. With the increasing number of renewable energy sources and the decrease in synchronous generators, which are a significant factor in creating a strong grid, these converters may not be suitable for future applications [7]. To address these issues, GFM control strategies have been proposed to enhance the stability of the VSC system under weak grid conditions [8]. While GFM converters offer stable operation for weak grid conditions and other advantages (such as fault ride through), they suffer from slower post-fault recovery due to virtual inertia and high fault current due to the lack of inner layer current controls [9]. Therefore, a control strategy that

can easily switch between different GFM and GFL strategies is crucial. Another reason for hybrid grid control strategies is that in an MTDC grid network, you need one terminal or MMC station to provide the DC voltage reference for the DC transmission network and to charge the cables.

A hybrid dynamical system consisting of a family of continuous-time subsystems and a rule governing the switch is called a switched system [10]. In this article, this term is renamed for clarification to highlight the application of this concept as a **Hybrid Control Strategy (HCS)**. This research article explores an HCS that combines the advantages of different control strategies into a single approach. In [11], the authors use a switching sequence based on the rate of change of frequency (RoCoF) and frequency change to detect disturbances and change the control strategies from GFM and GFL and vice versa. However, this research is only carried out for small increments in step changes or small signal changes. In [12], the authors propose a novel switching approach that matches the reference of the inner current loops for the GFL and GFM strategies by using the grid power synchronization loop. However, it requires the steady-state operating points to be the same before and after the control strategy switch. In [13], the authors propose a unified control loop to smoothly transition between grid-connected (GFL) mode and stand-alone (GFM) mode by defining the voltage and frequency ranges for each of the modes.

In this paper, the HCS proposes switching criteria based on the stability boundaries to adaptively optimize the operation of the converters in response to varying grid conditions for enhanced system performance, such as during transient fault events, their recovery, and post-transient states. This article uses Polytopic Lyapunov functions (PLFs) to achieve the switching strategy. The PLF approach allows for mode transitions, ensuring stability even under arbitrary fault-induced switching, resulting in a larger stability region and improved resilience against disturbances [14]. Furthermore, it reduces the chattering around the nominal operating point. The stability boundaries of PLFs form hyperplanes in which entities such as i_d, and i_q are surfaces forming a polytope in a 2-dimensional space. The boundary will be in the shape of a quadrilateral. In the literature, it has been used to give the modulated signal to ĆUK and SEPIC DC-DC converters [15], [16]. In this paper [15], the polytopic control approach is applied to the switched model of the power electronic-based system (ĆUK converter). This approach synthesizes the switching control signal using a Lyapunov function, with polytopic level sets. The PLFs can be viewed as concatenations of multiple linear functions or piecewise linear functions [17], making these functions not differentiable everywhere. This issue can be treated similarly to problems with the infinity or piecewise linear norm or by using Filippov's calculus for discontinuous differential equations [15], [18].

Furthermore, Section II deals with the network model on which the HCS is implemented. Sections III and IV discuss the two control strategies employed in the HCS. Section V delves into the mathematical implementation of PLF-based control switching. Section VI deals with the grid strength of the AC network and how this affects the control strategy selection. Lastly, Section VII discusses the real-time results of a HCS implementation and the meaningful conclusion.

II. NETWORK MODEL

Fig. 1 shows a four-terminal ±525 kV bipolar half-bridge MMC-based HVdc system with a metallic return and a DC Hub. The network specifications are given in Table 1 as reported in [19]. The modeled network is radial in topology, with two onshore stations, an onshore DC Hub (the central node in the radial topology), and two offshore stations connected to Wind Power Parks (WPPs). Furthermore, each station consists of two MMCs in a bipolar configuration. The analysis is only done for one of the converters in the bipolar configuration because, in this study, it is observed that the negative MMC mimics the behavior of the positive MMC (with the opposite sign but the same magnitude). This is because it is a symmetrical and balanced configuration, implying that each pole is at the same voltage, and the power delivered to and from the poles is the same.

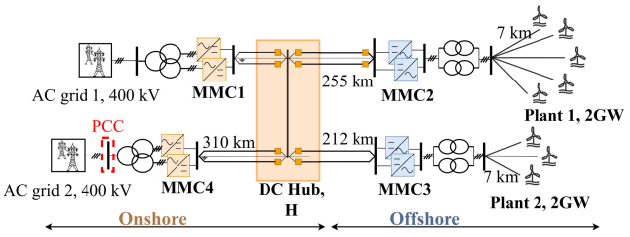

FIGURE 1. A four-terminal ±525 kV bipolar half-bridge MMC-based HVdc system with a metallic return and a DC Hub.

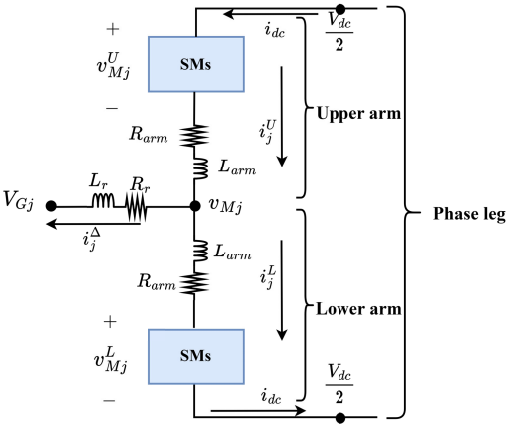

FIGURE 2. Diagram of one MMC leg, for $j \in \{a, b, c\}$.

Each MMC consists of three legs and two arms in each leg. N_{SM} is the number of submodules (SM) in every arm of the MMC. The variables shown in Fig. 2 are defined for the three legs (one leg for every phase), i.e., $j \in \{a, b, c\}$. Half-bridge submodules (SMs) are modeled using their averaged representations, with R_{arm} and L_{arm} being the equivalent resistance

TABLE 1. Network specifications.

Parameter	Onshore	Offshore
Transformer capacity	6 GW	4 GW
Rated grid line-line voltage	400 kV	66 kV
Transformer voltage ratio	400/275 kV	275/66 kV
Transformer leakage reactance	0.18 pu	0.15 pu
Transformer configuration	Yn/Δ, 1P3W	Δ/Yn, 3P2W
DC line inductances	80 mH	80 mH
No. of MMC Submodules	240	240
Submodule capacitance	25 mF	16 mF
Converter Inductance	50 mH	50 mH

and inductance, respectively. Each SM has capacitance C_{SM}. The converter model is developed according to [20], [21] and using $\Sigma - \Delta$ nomenclature, all the variables in the upper and lower arms of the converters can be represented as:

$$i_j^{\Delta} = i_j^U - i_j^L, \quad i_j^{\Sigma} = \frac{i_j^U + i_j^L}{2}, \tag{1}$$

$$v_{Mj}^{\Delta} = \frac{-v_{Mj}^U + v_{Mj}^L}{2}, \quad v_{Mj}^{\Sigma} = \frac{v_{Mj}^U + v_{Mj}^L}{2}. \tag{2}$$

By applying the Clarke-Park Transform to transform three-phase quantities (ABC) into direct-quadrature (dqZ) frame [20], the set of differential equations can be written in the dq-domain as:

$$\frac{d}{dt}\left(\vec{i}_{dq}^{\Delta}\right) = \frac{\vec{v}_{Mdq}^{\Delta} - \left(\omega L_{eq}^{ac} J_2 + R_{eq}^{ac} I_2\right)\vec{i}_{dq}^{\Delta} - \vec{V}_{Gdq}}{L_{eq}^{ac}}, \tag{3}$$

$$\frac{d}{dt}\left(\vec{v}_{dq}^{\Delta}\right) = \omega J_2 \vec{v}_{qd}^{\Delta} + \frac{N_{SM}}{C_{SM}}\vec{i}_{dq}^{\Delta}, \tag{4}$$

where $L_{eq}^{ac} = L_r + \frac{L_{arm}}{2}$, $R_{eq}^{ac} = R_r + \frac{R_{arm}}{2}$, $J_2 = \begin{bmatrix} 0 & 1 \\ -1 & 0 \end{bmatrix}$, and I_2 is an identity matrix with the size 2×2. Furthermore, the vector $\Delta\vec{x}(k) = \left[i_d^{\Delta},\ i_q^{\Delta}\right]^T$ represents state space variables and $\Delta\vec{u}(k) = \left[v_{Md}^{\Delta} - V_{Gd}, v_{Mq}^{\Delta} - V_{Gq}\right]^T$ input variables, where the subscript B represents the negative or lower MMC in the bipolar configuration. State-space matrices are:

$$A = \begin{bmatrix} -\frac{R_{eq}^{ac}}{L_{eq}^{ac}} & -\omega & 0 & 0 \\ \omega & -\frac{R_{eq}^{ac}}{L_{eq}^{ac}} & 0 & 0 \end{bmatrix} \tag{5}$$

$B = \text{diag}\left\{\frac{1}{L_{eq}^{ac}}, \frac{1}{L_{eq}^{ac}}\right\}$. This is the state-space representation of the inner control loop or cascaded current control loop of MMC-control strategies. Also, ω is denoted as ω_{GFL} for the GFL control strategy, as it is the output of a PLL unit; ω is denoted as ω_{GFM} for the GFM control strategy, as it is the output of a swing equation of a Virtual Synchronous Machine.

III. CONTROL STRATEGIES IMPLEMENTED: GFL

GFL converters are designed to supply active and reactive power to the grid and can be represented as a current-controlled source with high parallel impedance. However, one of the drawbacks of these converters is that they require perfect synchronization with the AC voltage of the grid at the PCC to regulate the exchange of active and reactive power accurately. This is achieved using the PLL to synchronize with the nominal frequency. However, this synchronization process can lead to instability problems when the grid weakens. In such cases, the PLL may be unable to maintain synchronization, leading to fluctuations in the exchanged power and affecting the system's stability [22]. To operate correctly, GFL converters need an external source to form the grid voltage at the PCC, and they cannot function in islanded mode. The operation of the GFL converters is often regulated by a high-level controller (outer control loop) like a Maximum Power Point Tracking (MPPT) controlled or a power plant controller, which sets the reference values of either P^*,[1] V_{dc}^*, Q^* and V_{ac}^* (V_{rms}^*). The inner control loop controls and regulates the currents injected into the grid by controlling the i_d and i_q currents [23].

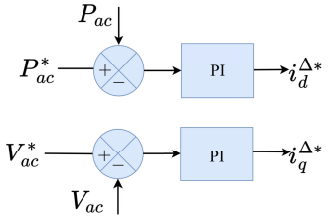

FIGURE 3. GFL control strategy.

A. STATE-SPACE REPRESENTATION, GFL: MONOPOLAR MMC CONFIGURATION

The type of GFL control strategy implemented is active power control for the d-axis and AC voltage control for the q-axis (outer loop). The state space equations representing the GFL control strategies are shown as follows: equation 6 and 7 are the outer loop state space equations, and equation 8 and 9, are the inner loop state space equations, respectively. Henceforth, * denotes the reference value or set point.

$$\dot{\xi}_{P_{ac}} = P_{ac}^* - P_{ac}, \tag{6}$$

$$\dot{\xi}_{V_{ac}} = V_{ac}^* - V_{ac}, \tag{7}$$

$$i_d^{*\Delta} = K_P^{P_{ac}}\left(P_{ac}^* - P_{ac}\right) + K_I^{P_{ac}}\xi_{P_{ac}}, \tag{8}$$

$$i_q^{*\Delta} = -K_P^{V_{ac}}\left(V_{ac}^* - V_{ac}\right) - K_I^{V_{ac}}\xi_{V_{ac}}, \tag{9}$$

$$\Delta x = \left[\xi_{P_{ac}},\ \xi_{V_{ac}}\right]^T. \tag{10}$$

[1] X^* denotes the reference value (setpoint) of X.

Combining the inner and outer loops' state-space equations of the GFL control strategies, we get new state space matrices:

$$A = \begin{bmatrix} -\frac{R_{eq}^{ac}}{L_{eq}^{ac}} & -\omega_{GFL} & 0 & 0 \\ \omega_{GFL} & -\frac{R_{eq}^{ac}}{L_{eq}^{ac}} & 0 & 0 \\ 0 & 0 & K_I^{P_{ac}} & 0 \\ 0 & 0 & 0 & -K_I^{V_{ac}} \end{bmatrix}, \tag{11}$$

$$B = \text{diag}\left\{ \frac{1}{L_{eq}^{ac}}, \frac{1}{L_{eq}^{ac}}, -K_P^{P_{ac}}, K_P^{V_{ac}} \right\}, \tag{12}$$

$$\vec{\Delta}x(k) = \left[i_d^{\Delta}, i_q^{\Delta}, \xi_{P_{ac}}, \xi_{V_{ac}} \right]^T, \tag{13}$$

$$\vec{\Delta}u(k) = \left[v_{Md}^{\Delta} - V_{Gd}, v_{Mq}^{\Delta} - V_{Gq}, \left(P_{ac}^* - P_{ac}\right), \left(V_{ac}^* - V_{ac}\right) \right]^T. \tag{14}$$

IV. CONTROL STRATEGIES IMPLEMENTED: GFM

The GFM control strategy is relatively new and has not been implemented in real-life transmission networks [24]. GFM controls can be represented as a voltage-controlled source with low series impedance. They are mainly designed to set the voltage and frequency of the network in the PCC [25]. These voltage source converters need not be perfectly synchronized with the AC voltage of the grid, as they generate their phase angle and, therefore, can operate in islanded mode. The operation of the GFM converters is often regulated by a voltage reference V_{AC}^* (V_{rms}^*, outer loop) and frequency set points. This control strategy usually does not require inner current ($i_{d,q}$) control when additional protection equipment is already used in the network [26].

For GFM converter controls, a Virtual Synchronous Machine (VSM) with cascaded dual-layer current control, augmented by a virtual capacitance, is implemented [27]. This virtual capacitance accomplishes a crucial function, namely, it decouples the voltage loop and facilitates the generation of i_d and i_q references within this control framework [27]. This makes the switching algorithm simpler and easier to implement.

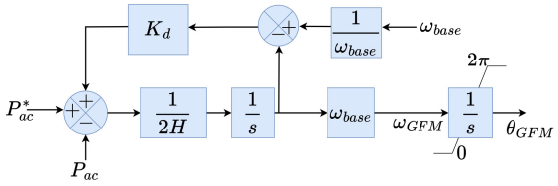

FIGURE 4. VSM theta generation schematic.

A. STATE-SPACE REPRESENTATION, GFM: MONOPOLAR MMC CONFIGURATION

The outer loop of the GFM control strategy is revised with a virtual capacitor to decouple the dq voltages and implement a cascading dq current control. Equation 15 and 16 represent the outer loop state space equations of the GFM control strategy, and equations (17) and (18), represent the inner loop state space equations of the GFM control strategy respectively.

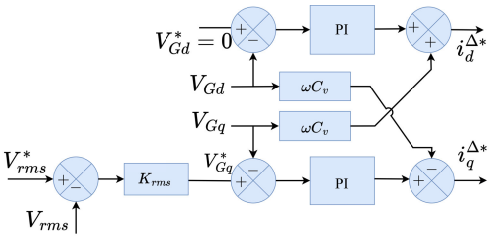

FIGURE 5. Modified GFM-VSM control strategy with virtual capacitance.

$$\dot{\xi}_{V_{Gd}} = V_{Gd}^* - V_{Gd}, \tag{15}$$

$$\dot{\xi}_{V_{Gq}} = V_{Gq}^* - V_{Gq}, \tag{16}$$

here, $V_{Gd}^* = 0$ and $V_{Gq}^* = K_{rms}\left(V_{rms}^* - V_{rms}\right)$. And

$$i_d^{*\Delta} = K_P^{dGFM}\left(V_{Gd}^* - V_{Gd}\right) + K_I^{dGFM}\xi_{V_{Gd}} - \omega C_v\left(V_{Gq}^* - V_{Gq}\right) + \omega C_v V_{Gq}^*, \tag{17}$$

$$i_q^{*\Delta} = K_P^{qGFM}\left(V_{Gq}^* - V_{Gq}\right) - K_I^{qGFM}\xi_{V_{Gq}} + \omega C_v\left(V_{Gd}^* - V_{Gd}\right) - \omega C_v V_{Gd}^*, \tag{18}$$

$$\Delta x = \left[\xi_{V_{Gd}}, \xi_{V_{Gq}} \right]^T, \tag{19}$$

combine the inner loop and the outer loop state space equations of the GFM control strategies, so that we get new state space matrices:

$$A = \begin{bmatrix} -\frac{R_{eq}^{ac}}{L_{eq}^{ac}} & -\omega_{GFM} & 0 & 0 \\ \omega_{GFM} & -\frac{R_{eq}^{ac}}{L_{eq}^{ac}} & 0 & 0 \\ 0 & 0 & K_I^{dGFM} & 0 \\ 0 & 0 & 0 & -K_I^{qGFM} \end{bmatrix}, \tag{20}$$

$$B = \begin{bmatrix} \frac{1}{L_{eq}^{ac}} & 0 & 0 & 0 \\ 0 & \frac{1}{L_{eq}^{ac}} & 0 & 0 \\ 0 & 0 & -K_p^{dGFM} & -\omega C_v \\ 0 & 0 & \omega C_v & K_p^{qGFM} \end{bmatrix}, \tag{21}$$

$$G = \begin{bmatrix} 0 & 0 & 0 & 0 \\ 0 & 0 & 0 & 0 \\ 0 & 0 & 0 & \omega C_v \\ 0 & 0 & -\omega C_v & 0 \end{bmatrix}, \tag{22}$$

$$\vec{\Delta}x(k) = \left[i_d^{\Delta}, \quad i_q^{\Delta}, \xi_{V_{Gd}}, \quad \xi_{V_{Gq}} \right]^T, \tag{23}$$

$$\vec{\Delta}u(k) = \begin{bmatrix} v_{Md}^{\Delta} - v_d^G, v_{Mq}^{\Delta} - v_q^G, \left(V_{Gd}^* - V_{Gd}\right), \\ \left(V_{Gq}^* - V_{Gq}\right) \end{bmatrix}^T. \tag{24}$$

Vector $\vec{\Delta}q(k) = \left[0, 0, V_{Gd}^*, V_{Gq}^*\right]^T$, this being a set-point, it is constant.

V. PLF-BASED HYBRID CONTROL METHODOLOGY

Let us consider that the steady-state values of the states from the state space equations are denoted by $\bar{x}_{GFL}$ and $\bar{x}_{GFM}$.

They are calculated for GFL control as:

$$\bar{x}_{GFL} = \left[\bar{i}_d^{\Delta}, \quad \bar{i}_q^{\Delta}, \bar{\xi}_{P_{ac}}, \quad \bar{\xi}_{V_{ac}} \right]^T \tag{25}$$

The values of $\dot{\bar{\xi}}_{P_{ac}}$ and $\dot{\bar{\xi}}_{V_{ac}}$ are equal to zero, as the steady state value of the errors is 0. Therefore, the values of $\bar{\xi}_{P_{ac}}$ and $\bar{\xi}_{V_{ac}}$ are constants (C_i).

$$\bar{x}_{GFL} = \left[\bar{i}_d^{\Delta}, \bar{i}_q^{\Delta}, C_{P_{ac}}, C_{V_{ac}} \right]^T. \tag{26}$$

One may note that steady-state values given as $\bar{\cdot}$ are ideally equal to the reference value $(\cdot)^*$. This notation is applied to generalize the control design.

Similarly,

$$\bar{x}_{GFM} = \left[\bar{i}_d^{\Delta}, \bar{i}_q^{\Delta}, \bar{\xi}_{V_{Gd}}, \bar{\xi}_{V_{Gq}} \right]^T, \tag{27}$$

where the values of $\dot{\bar{\xi}}_{V_{Gd}}$ and $\dot{\bar{\xi}}_{V_{Gq}}$ are equal to zero, as the steady state value of the errors is 0. Therefore, the values of $\bar{\xi}_{V_{Gd}}$&$\bar{\xi}_{V_{Gq}}$ are constants (C_i).

Furthermore, the steady-state values of GFM are:

$$\bar{x}_{GFM} = \left[\bar{i}_d^{\Delta}, \bar{i}_q^{\Delta}, C_{V_{Gd}}, C_{V_{Gq}} \right]^T. \tag{28}$$

Now, let us define the system variables around its steady-state as:

$$y = x - \bar{x}$$

which for GFL control is:

$$y_{GFL} = \begin{bmatrix} i_d^{\Delta} - \bar{i}_d^{\Delta} \\ i_q^{\Delta} - \bar{i}_q^{\Delta} \\ \xi_{P_{ac}} - C_{P_{ac}} \\ \xi_{V_{ac}} - C_{V_{ac}} \end{bmatrix} \tag{29}$$

and for GFM control:

$$y_{GFM} = \begin{bmatrix} i_d^{\Delta} - \bar{i}_d^{\Delta} \\ i_q^{\Delta} - \bar{i}_q^{\Delta} \\ \xi_{V_{Gd}} - C_{V_{Gd}} \\ \xi_{V_{Gq}} - C_{V_{Gq}} \end{bmatrix} \tag{30}$$

To be able to incorporate these changes in the ordinary differential equations describing the operation of GFM and GFL controls, the ordinary differential equations can be rewritten as:

$$\dot{y}_j = A_j(x - \bar{x}) + A_j\bar{x} + B_j = A_j y_j + \bar{B}_j, \tag{31}$$

where A_j, for $j \in \{GFL, GFM\}$, is the same as in(11) and (20), respectively, and, $\bar{B}_j = A_j\bar{x}_j + B_j$ is:

$$\bar{B}_{GFL} = \begin{bmatrix} -\frac{R_{eq}^{ac}}{L_{eq}^{ac}}\bar{i}_d^{\Delta} - \omega_{GFL}\bar{i}_q^{\Delta} + \frac{1}{L_{eq}^{ac}}\left(v_{Md}^{\Delta} - v_d^G\right) \\ -\frac{R_{eq}^{ac}}{L_{eq}^{ac}}\bar{i}_q^{\Delta} + \omega_{GFL}\bar{i}_d^{\Delta} + \frac{1}{L_{eq}^{ac}}\left(v_{Mq}^{\Delta} - v_q^G\right) \\ K_I^{P_{ac}} C_{P_{ac}} \\ -K_I^{V_{ac}} C_{V_{ac}} \end{bmatrix}, \tag{32}$$

and

$$\bar{B}_{GFM} = \begin{bmatrix} -\frac{R_{eq}^{ac}}{L_{eq}^{ac}}\bar{i}_d^{\Delta} - \omega_{GFM}\bar{i}_q^{\Delta} + \frac{1}{L_{eq}^{ac}}\left(v_{Md}^{\Delta} - v_d^G\right) \\ -\frac{R_{eq}^{ac}}{L_{eq}^{ac}}\bar{i}_q^{\Delta} + \omega_{GFM}\bar{i}_d^{\Delta} + \frac{1}{L_{eq}^{ac}}\left(v_{Mq}^{\Delta} - v_q^G\right) \\ K_I^{dGFM} C_{V_{Gd}} \\ -K_I^{qGFM} C_{V_{Gq}} \end{bmatrix}. \tag{33}$$

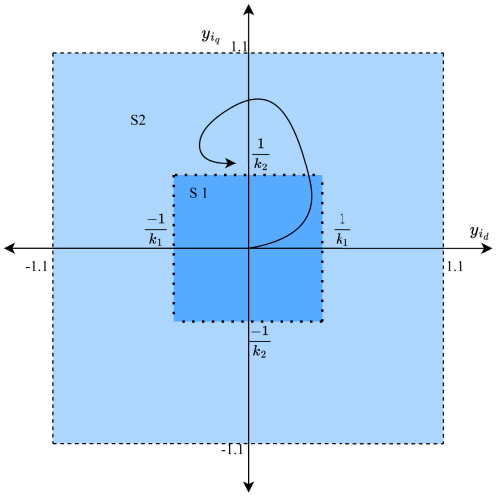

FIGURE 6. Polytope representation of the switching, where SS1 and SS2 represent the two states.

Let us define the PLF using the infinity norm on the first two variables. In this article, the effect of the other two states is not considered, as they do not contribute significantly to the behavior of the control strategies:

$$V(y) = \max_{i \in \{1,2\}} \{|k_i y_i|\} \tag{34}$$

where $i \in I = \{GFL, GFM\}$. Then the polytope, as seen from Fig. 6, is defined as:

$$\mathbf{P} = \left\{ y \in \mathbf{R}^2 : |k_i y_i| \leq 1, i \in \{1, 2\} \right\} \tag{35}$$

With the switching law as observed in Fig. 6:

$$q = \begin{cases} 0 & \text{if 1 and } k_i y_i \geq 1, \\ \{0, 1\} & \text{if } \{0, 1\} \text{ and } -1 < k_i y_i < 1, \quad i \in \{1, 2\}. \\ 1 & \text{if 0 and } k_i y_i \leq -1. \end{cases} \tag{36}$$

Assuming that for $j \in \{1, 2\}$, the Lyapunov function has a maximum positive value, then to have a stable system operation, its derivative must be negative, such as:

$$V(y) = \left|k_j y_j\right| = k_j y_j \operatorname{sgn}\left(k_j y_j\right), \tag{37}$$

$$\begin{aligned} \dot{V}_i(y) &= k_j \dot{y}_j \operatorname{sgn}\left(k_j y_j\right) \\ &= k_j \operatorname{sgn}\left(k_j y_j\right) \left(A_i\langle j, 1:4\rangle y_i + \bar{B}_i\langle j\rangle\right). \end{aligned} \tag{38}$$

To obtain proper operation at the facets of the polytope, the coefficients k_i must satisfy the maximum allowed error

values [15], and the $\frac{1}{k_i}$ can be interpreted as the stability margins the respective control strategies:

$$k_i = \pm|y_i| \text{ or } \frac{1}{k_i} = \pm\frac{1}{|y_i|} \tag{39}$$

The sign of the coefficient must be determined to obtain the proper system operation by analyzing the Lyapunov control function and its derivative.

Therefore, for GFL control, we have:

$$\frac{1}{k_{GFL,1}} = \pm\frac{1}{|i_d^\Delta - \bar{i}_d^\Delta|}, \quad \frac{1}{k_{GFL,2}} = \pm\frac{1}{|i_q^\Delta - \bar{i}_q^\Delta|}, \tag{40}$$

And for GFM:

$$\frac{1}{k_{GFM,1}} = \pm\frac{1}{|i_d^\Delta - \bar{i}_d^\Delta|}, \quad \frac{1}{k_{GFM,2}} = \pm\frac{1}{|i_q^\Delta - \bar{i}_q^\Delta|}. \tag{41}$$

Assumption: the switch from GFL to GFM is **positive** and the switch from GFM to GFL is **negative**.

Let us now analyze the derivative of the Lyapunov function for both the GFL and GFM control modes when one of the corresponding variables provides the maximum value of the Lyapunov function, that is, $j = \arg\max_{i\in I}\{|k_i y_i|\}$.

Consider switching cases that might occur.

A. THE SWITCH TO GFL CONTROL IS VALID AND $k_{GFL,1}$ HAS A MAXIMUM VALUE

The derivative of the PLF in this case is given as:

$$\dot{V}_{GFL}(y) = -k_{GFL,1}\left(A_{GFL}\langle 1, 1:4\rangle y_{GFL} + \overline{B}_{GFL}\langle 1\rangle\right), \tag{42}$$

$$\dot{V}_{GFL}(y) = -k_{GFL,1}\left(-\frac{R_{eq}^{ac}}{L_{eq}^{ac}} i_d^\Delta - \omega_{GFL} i_q^\Delta + \frac{1}{L_{eq}^{ac}}\left(v_{Md}^\Delta - v_d^G\right)\right) < 0. \tag{43}$$

Now, if we consider that $k_{GFL,1} > 0$ then,

$$\frac{R_{eq}^{ac}}{L_{eq}^{ac}} i_d^\Delta + \omega_{GFL} i_q^\Delta < \frac{1}{L_{eq}^{ac}}\left(v_{Md}^\Delta - v_d^G\right),$$

which holds when i_d^Δ, i_q^Δ are positive values since $v_{Md}^\Delta - v_d^G > 0$. This argument is further solidified by substituting the numerical values from Table 2. Namely,

$$0.02 i_d^\Delta + i_q^\Delta < 0.5246 \tag{44}$$

and after substituting the dq current values obtained from simulations, one can see that the relation is correct. For $k_{GFL,1} < 0$,

$$\frac{R_{eq}^{ac}}{L_{eq}^{ac}} i_d^\Delta + \omega_{GFL} i_q^\Delta > \frac{1}{L_{eq}^{ac}}\left(v_{Md}^\Delta - v_d^G\right),$$

this condition is not possible as $v_{Md}^\Delta - v_d^G$ is positive, and according to the dq current values from the simulations is not possible.

TABLE 2. MMC setpoints and simulated values.

Quantity	Value	Quantity	Value
P^*	$1pu$	V_{rms}^*	$1pu$
L_{eq}^{ac}:	$0.15pu$	R_{eq}^{ac}:	$0.0034pu$
GFL, $\overline{V_d^M}$	$0.787pu$	GFL, $\overline{V_q^M}$	$0.787pu$
GFL, $\overline{V_d}$	$0.63pu$	GFL, $\overline{V_q}$	$0.032pu$
GFL, $\overline{i_d^*}$	$0.59pu$	GFL, $\overline{i_q^*}$	$0.06pu$
GFL, $\overline{i_d}$	$0.59pu$	GFL, $\overline{i_q}$	$0.06pu$
GFL,$K_I^{P_{ac}}$	$0.2s$	GFL,$K_I^{V_{ac}}$	$0.25s$
GFL,$K_P^{P_{ac}}$	$0.1pu$	GFL,$K_P^{V_{ac}}$	$0.09pu$
GFM, $\overline{V_d^M}$	$0.578pu$	GFM, $\overline{V_q^M}$	$0.6452pu$
GFM, $\overline{V_d}$	$0.554pu$	GFM, $\overline{V_q}$	$0.833pu$
GFM, $\overline{i_d^*}$	$-0.12pu$	GFM, $\overline{i_q^*}$	$-0.156pu$
GFM, $\overline{i_d}$	$-0.12pu$	GFM, $\overline{i_q}$	$-0.156pu$
GFM,K_I^{dGFM}	$0.37s$	GFM,K_I^{qGFM}	$0.43s$
GFM,K_P^{dGFM}	$0.17pu$	GFM,K_P^{qGFM}	$0.11pu$

B. THE SWITCH TO GFM CONTROL IS VALID AND $k_{GFM,1}$ HAS A MAXIMUM VALUE

Again, we look at the PLF time derivative in this case:

$$\dot{V}_{GFM}(y) = k_{GFM,1}\left(A_{GFM}\langle 1, 1:4\rangle y_{GFM} + \overline{B}_{GFM}\langle 1\rangle\right), \tag{45}$$

$$\dot{V}_{GFM}(y) = k_{GFM,1}\left(-\frac{R_{eq}^{ac}}{L_{eq}^{ac}} i_d^\Delta - \omega_{GFM} i_q^\Delta + \frac{1}{L_{eq}^{ac}}\left(v_{Md}^\Delta - v_d^G\right)\right) < 0. \tag{46}$$

Now, first we consider $k_{GFM,1} > 0$ then,

$$\frac{R_{eq}^{ac}}{L_{eq}^{ac}} i_d^\Delta + \omega_{GFM} i_q^\Delta > \frac{1}{L_{eq}^{ac}}\left(v_{Md}^\Delta - v_d^G\right)$$

which holds when i_d^Δ, i_q^Δ and $v_{Md}^\Delta - v_d^G$ are negative values. When replacing the numerical values from Table 2, this becomes:

$$0.02 i_d^\Delta + i_q^\Delta > -0.16. \tag{47}$$

For $k_{GFM,1} < 0$,

$$-\frac{R_{eq}^{ac}}{L_{eq}^{ac}} i_d^\Delta - \omega_{GFM} i_q^\Delta > -\frac{1}{L_{eq}^{ac}}\left(v_{Md}^\Delta - v_d^G\right)$$

this condition is not possible as $v_{Md}^\Delta - v_d^G$ is negative.

C. THE SWITCH TO GFL CONTROL IS VALID AND $k_{GFL,2}$ HAS A MAXIMUM VALUE

$$\dot{V}_{GFL}(y) = -k_{GFL,2}\left(A_{GFL}\langle 2, 1:4\rangle y_{GFL} + \overline{B}_{GFL}\langle 2\rangle\right) \tag{48}$$

$$\dot{V}_{GFL}(y) = -k_{GFL,2}\left(-\frac{R_{eq}^{ac}}{L_{eq}^{ac}} i_q^\Delta - \omega_{GFL} i_d^\Delta + \frac{1}{L_{eq}^{ac}}\left(v_{Mq}^\Delta - v_q^G\right)\right) < 0 \tag{49}$$

Now, we consider $k_{GFL,2} > 0$ then,

$$\frac{-R_{eq}^{ac}}{L_{eq}^{ac}} i_q^{\Delta} + \omega_{GFL} i_d^{\Delta} > \frac{-1}{L_{eq}^{ac}} \left(v_{Mq}^{\Delta} - v_q^G \right)$$

which holds when i_d^{Δ}, i_q^{Δ} and $v_{Md}^{\Delta} - v_d^G$ are positive values. The same can be seen from the numerical values:

$$-0.02 i_q^{\Delta} + i_d^{\Delta} > -5.033. \tag{50}$$

For $k_{GFL,2} < 0$,

$$\frac{-R_{eq}^{ac}}{L_{eq}^{ac}} i_q^{\Delta} + \omega_{GFL} i_d^{\Delta} < \frac{-1}{L_{eq}^{ac}} \left(v_{Mq}^{\Delta} - v_q^G \right)$$

this condition is not possible as i_d^{Δ} is non-positive in this case.

D. THE SWITCH TO GFM CONTROL IS VALID AND $k_{GFM,2}$ HAS A MAXIMUM VALUE

$$\dot{V}_{GFM}(y) = k_{GFM,2} \left(A_{GFM} \langle 2, 1:4 \rangle y_{GFM} + \overline{B}_{GFM} \langle 2 \rangle \right) \tag{51}$$

$$\dot{V}_{GFM}(y) = k_{GFM,2} \left(-\frac{R_{eq}^{ac}}{L_{eq}^{ac}} i_q^{\Delta} + \omega_{GFM} i_d^{\Delta} + \frac{1}{L_{eq}^{ac}} \left(v_{Mq}^{\Delta} - v_q^G \right) \right) < 0 \tag{52}$$

Now, we consider $k_{GFM,2} > 0$ then,

$$-\frac{R_{eq}^{ac}}{L_{eq}^{ac}} i_q^{\Delta} + \omega_{GFM} i_d^{\Delta} < -\frac{1}{L_{eq}^{ac}} \left(v_{Mq}^{\Delta} - v_q^G \right)$$

which holds when i_d^{Δ}, i_q^{Δ} and $v_{Md}^{\Delta} - v_d^G$ are negative values values. The same can be seen from the numerical values:

$$-0.02 i_q^{\Delta} + i_d^{\Delta} < 1.252. \tag{53}$$

For $k_{GFM,2} < 0$,

$$-\frac{R_{eq}^{ac}}{L_{eq}^{ac}} i_q^{\Delta} - \omega_{GFM} i_d^{\Delta} > -\frac{1}{L_{eq}^{ac}} \left(v_{Mq}^{\Delta} - v_q^G \right)$$

this condition is not possible as $v_{Mq}^{\Delta} - v_q^G$ is negative.

With the above calculations, it is evident that the derivative of the PLF concerning time is negative outside the polytope region **P**. Checking the behavior of the system on switching hyperplanes where the derivative of the PLF does not exist is crucial for the overall stability of the system, which is carried out using the Filippov criterion [28], [29]. This is done by showing that the following differential inclusion inequality is satisfied for $\alpha, \beta \in [0, 1]$, on the hyperplanes [15].

$$\left(\beta \operatorname{grad} V(y)\big|_{GFL} + (1-\beta) \operatorname{grad} V(y)\big|_{GFM} \right) \mathrm{x} \left(\alpha \dot{x}\big|_{GFL} + (1-\alpha) \dot{x}\big|_{GFM} \right) < 0. \tag{54}$$

By calculating all the possible facets of the polytope, $(\frac{1}{K})$ for the control strategies, we obtain for GFL: $\frac{1}{k_{GFL,1}} = 0.15$, $\frac{1}{k_{GFL,2}} = 0.08$, and, for GFM: $\frac{1}{k_{GFM,1}} = 0.21$, $\frac{1}{k_{GFM,2}} = 0.11$. Therefore, if $\frac{1}{k_1} \leq 0.15$ and $\frac{1}{k_2} \leq 0.08$, the HCS chooses GFL and if $\frac{1}{k_1} \geq 0.21$ and $\frac{1}{k_2} \geq 0.11$, the HCS chooses GFM. The difference in the values of $\frac{1}{k_1}$ and $\frac{1}{k_2}$ are treated as buffer zones. For steady state, $\overline{e} \approx e^*$, where $*$ refers to the set point or reference value.

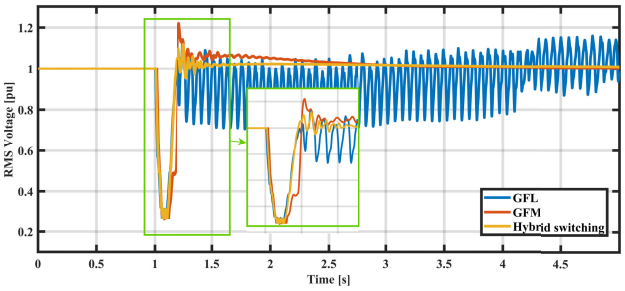

FIGURE 7. Comparison of control strategies for a Line-to-line fault.

The current design polytope results in frequent switching. This can be limited by implementing a minimum dwell time or introducing delays between switches [30], which would help mitigate these effects, which will be analyzed in future studies. These delays are inherently introduced by any programmable device used for control implementation.

VI. REAL-TIME RESULTS

A. SHORT CIRCUIT STRENGTH EFFECT

The grid strength or the Short Circuit Ratio (SCR) of the AC grid connected to the HVdc systems is the system strength at a particular bus, as the ratio between the short circuit power and the nominal power of the HVdc link connected to that bus [31]. For weak grid conditions (low SCR), the GFL control strategies are not an ideal choice due to AC voltage and frequency fluctuations [32]. Furthermore, GFM control strategies are less suitable when the grid is strong (high SCR), as they attempt to establish their own voltage and frequency references, leading to synchronization issues [32]. Here, two SCR cases are considered: SCR of 1.5 and 3.5 representing weak and strong grid scenarios, respectively. This is considered to test the HCS under different grid strengths, to show the robustness of the HCS as the trajectories of the state variables (in this case,$i_{d/q}$) are different under different grid conditions. Under ideal operating conditions (before and after the transient phenomena), the hybrid switching control strategy should opt for the GFM under weak grid conditions and GFL under strong grid conditions. During transient events, the HCS should opt for the control strategy that performs best in the particular situation, whether it be fault current limiting (GFL) or an inertial response (GFM). This is further demonstrated in practice with the help of transient phenomena.

B. FAULTS

All the faults or transient phenomena analysed in this subsection are initiated at $t_f = 1$s. Fig. 7 shows the merits

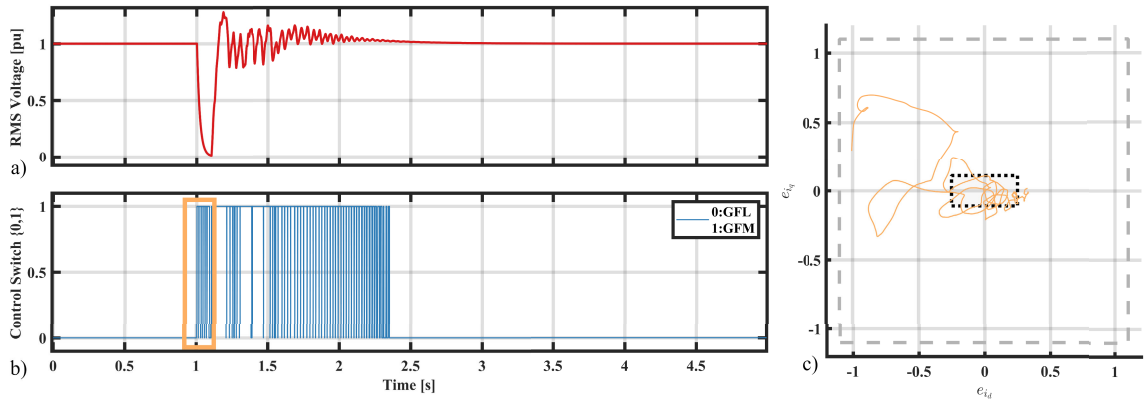

FIGURE 8. AC three-phase fault for SCR of 3.5.

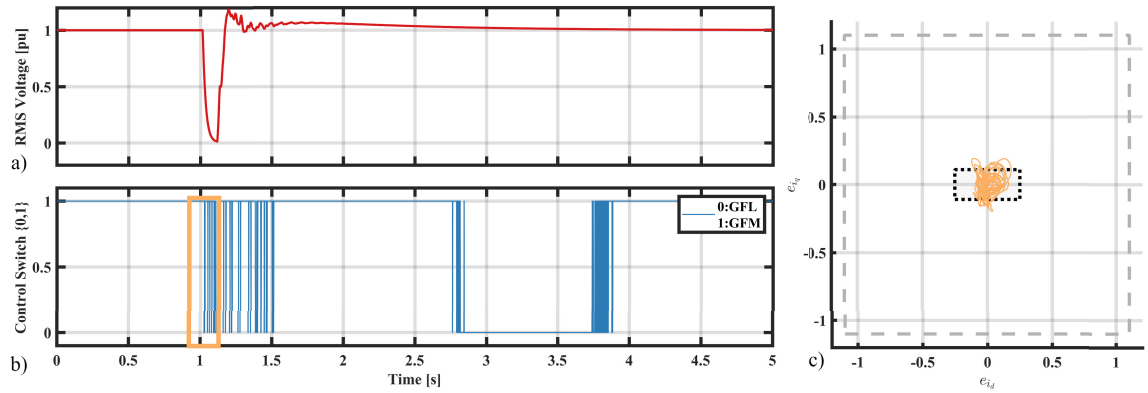

FIGURE 9. AC three-phase fault for SCR of 1.5.

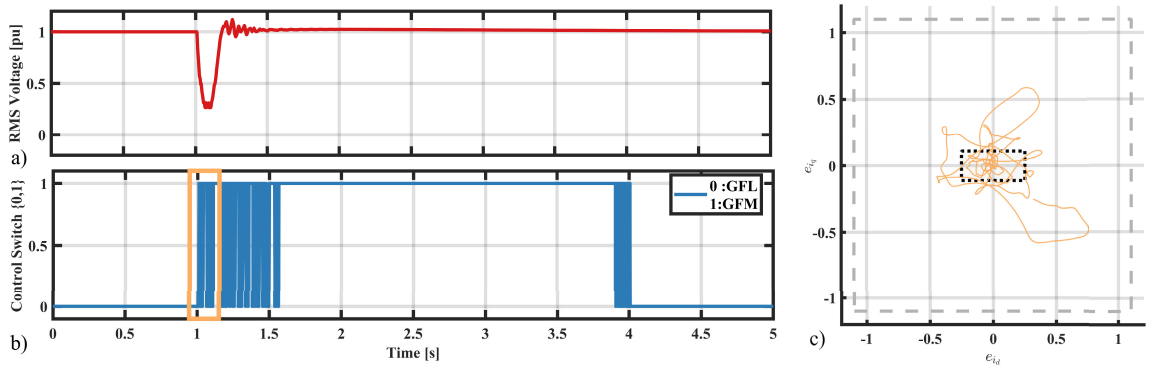

FIGURE 10. AC line-to-line fault for SCR of 3.5.

of using HCS over conventional GFM-only and GFL-only control strategies. The triggered fault is a line-to-line fault. It can be seen that the HCS recovers faster than the GFM-only converter, because after the fault is cleared, it switches to the GFL converter. However, again, it switches to the GFM mode to take advantage of the inertial characteristics of the GFM. Therefore, the HCS settles faster with very few oscillations.

For the figures that follow, Figs. 8-12, subfigures (a) show the V_{rms} curves of the transient event, subfigures (b) show the control switching actions of the HCS in response to the faults triggered, and (c) shows the trajectories of the corresponding dq current error values around and along the polytope boundaries that were calculated previously for a specific time interval t_{int} which is enclosed by a rectangle in subfigures (b).

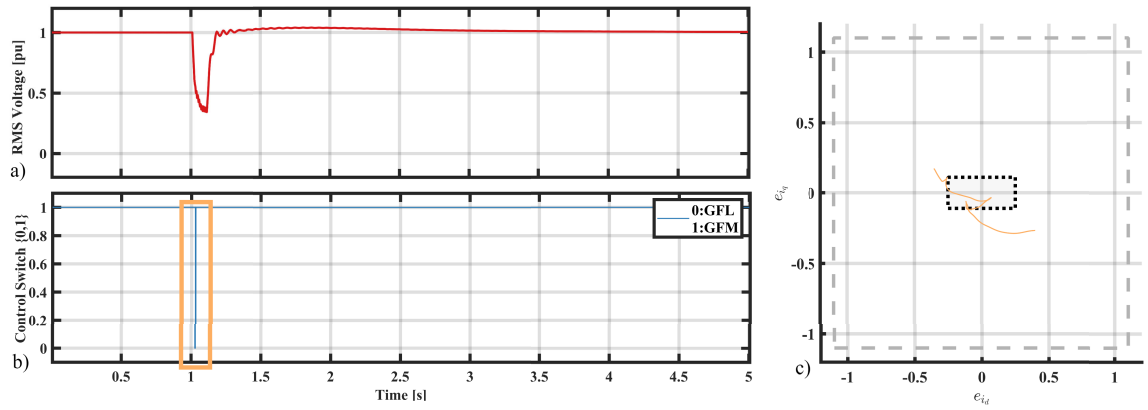

FIGURE 11. **AC line-to-line fault for SCR of 1.5.**

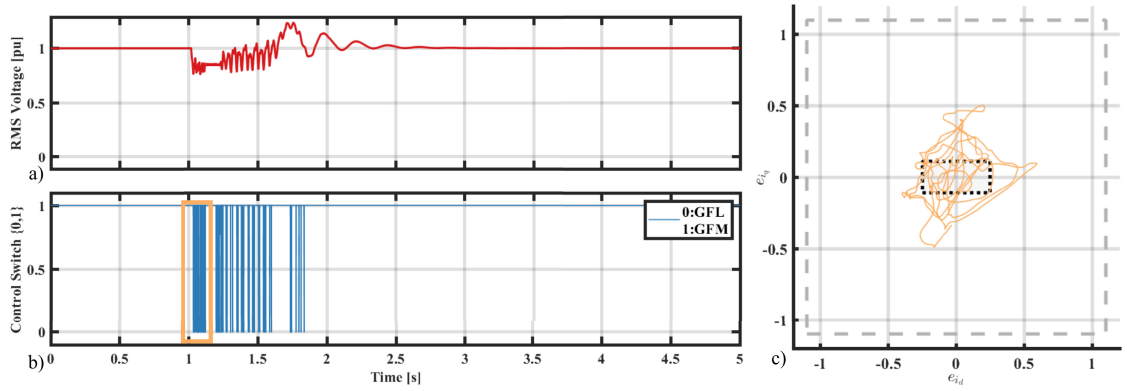

FIGURE 12. **AC single phase fault for SCR of 1.5.**

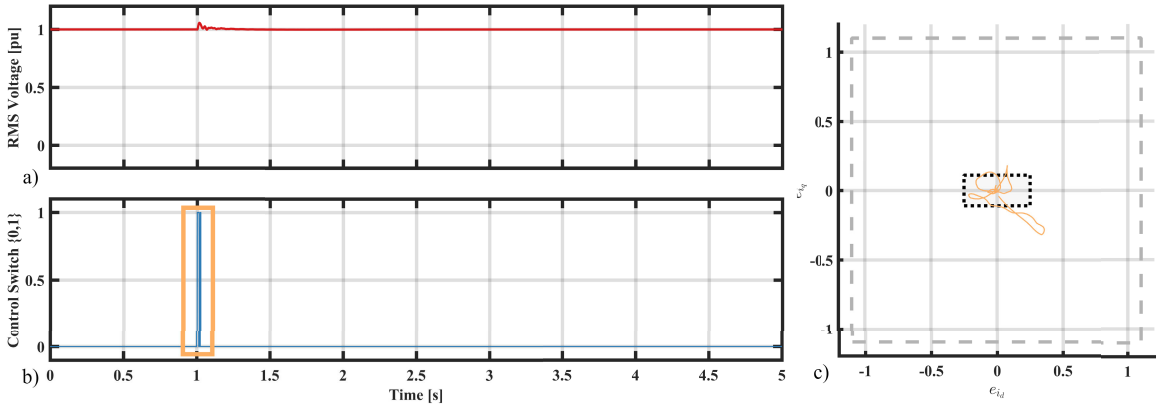

FIGURE 13. **AC phase jump for SCR of 3.5.**

Fig. 14 portrays the inner loop dq-current curves, and Fig. 15 shows the active power curves of all the transient events discussed.

Fig. 8 shows the trajectory of the curves for an SCR of 3.5, where GFL still works without big oscillations, and the triggered fault is a three-phase fault. It can be seen that the control strategy employed by the HCS is GFL, and in case of a fault, the controller switches between GFM and GFL to take advantage of each of the control strategies during the transient phenomena. Once the fault is completely cleared and the V_{rms} reached steady state, the HCS switches to GFL control, which is the control strategy the HCS used initially, depending on

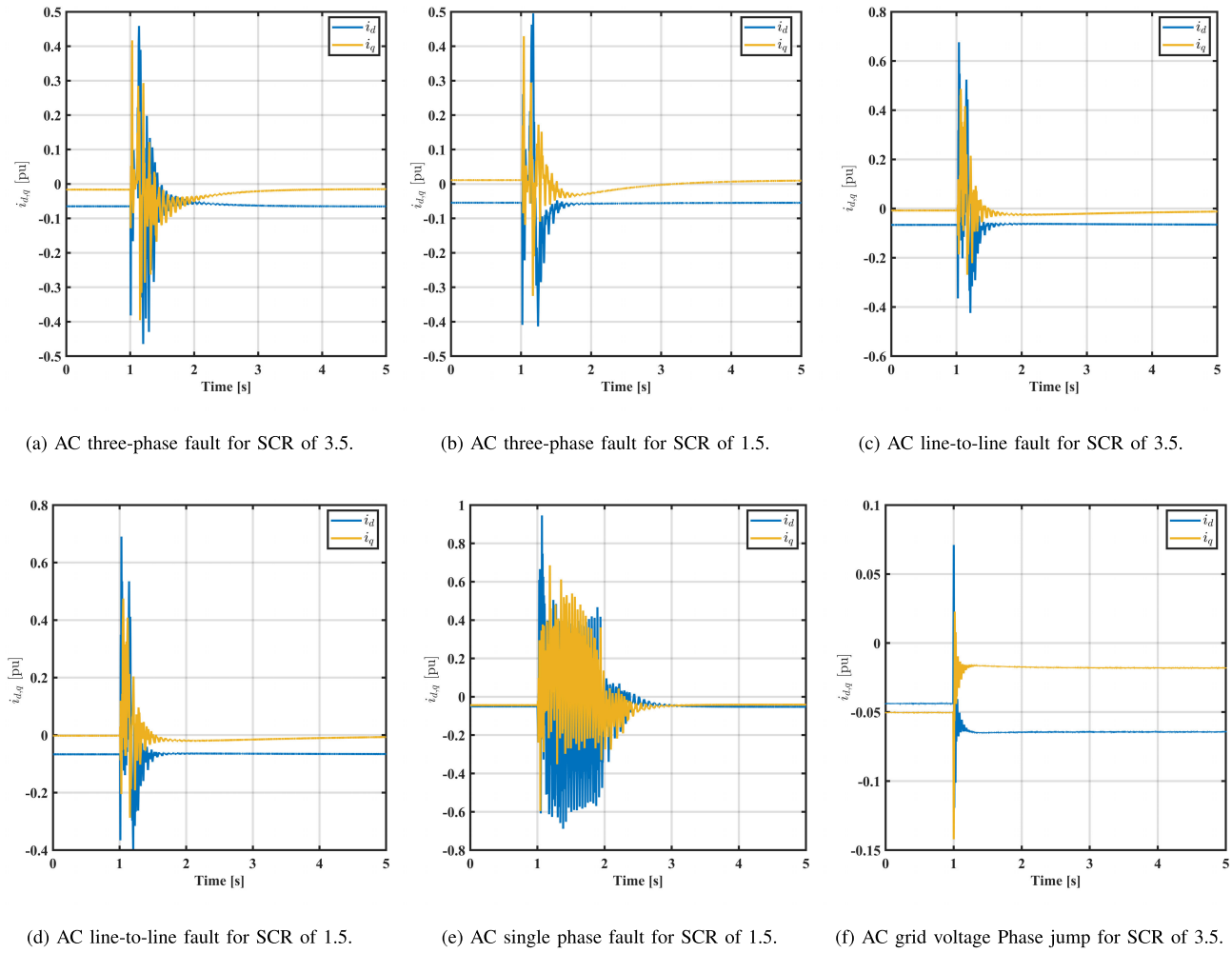

(a) AC three-phase fault for SCR of 3.5.

(b) AC three-phase fault for SCR of 1.5.

(c) AC line-to-line fault for SCR of 3.5.

(d) AC line-to-line fault for SCR of 1.5.

(e) AC single phase fault for SCR of 1.5.

(f) AC grid voltage Phase jump for SCR of 3.5.

FIGURE 14. Inner loop dq-currents during the respective transient phenomena.

the SCR. Fig. 14 shows the dq-current curves during the HCS action for the fault. Fig. 15 shows that the oscillations in the active power curve damp after the transient event during HCS action.

Fig. 9 shows the trajectory of the curves for an SCR of 1.5, where GFM works better than GFL for steady-state conditions, and the triggered fault is a three-phase fault. It can be seen that the control strategy employed by the HCS is GFM, and in case of a fault, the controller switches between GFM and GFL to take advantage of each of the control strategies during the transient phenomena. Once the fault is completely cleared and the V_{rms} reaches steady state, the HCS switches to GFM control, which is the control strategy the HCS used initially based on the SCR. It can also be seen that although from the V_{rms} curves in Fig. 9a, the oscillations are damped after about 1 s of the triggered fault, and the system appears to be stable, the system internally is only marginally stable and requires about 2 s more to reach the steady state. This study explains the nature of the converter stations, the control strategies, and the trajectories of the dq current errors. It provides more insight into the overall system as a whole. Fig. 14b shows the dq-current curves during the HCS action for the fault. Fig. 15b shows that the oscillations in the active power curve are dampened after the transient event during HCS action.

Fig. 10 shows the trajectory of the curves for an SCR of 3.5, where GFL still operates without showing high oscillations at steady states, and the fault triggered is a line-to-line fault. It can be seen that the control strategy employed by the HCS is GFL, and in case of a fault, the controller switches between GFL and GFM to take advantage of each of the control strategies during the transient phenomena. Once the fault is completely cleared and the V_{rms} has reached its steady state, the HCS switches to the GFL control, the one that the HCS used initially based on the SCR. It can also be seen that although from the V_{rms} curves in Fig. 10a, the oscillations are damped after about 0.5 s of the fault occurrence, and the system appears to be stable, the system internally is only marginally stable and requires nearly 2.5 s more to reach steady state. This study explains the nature of the converter

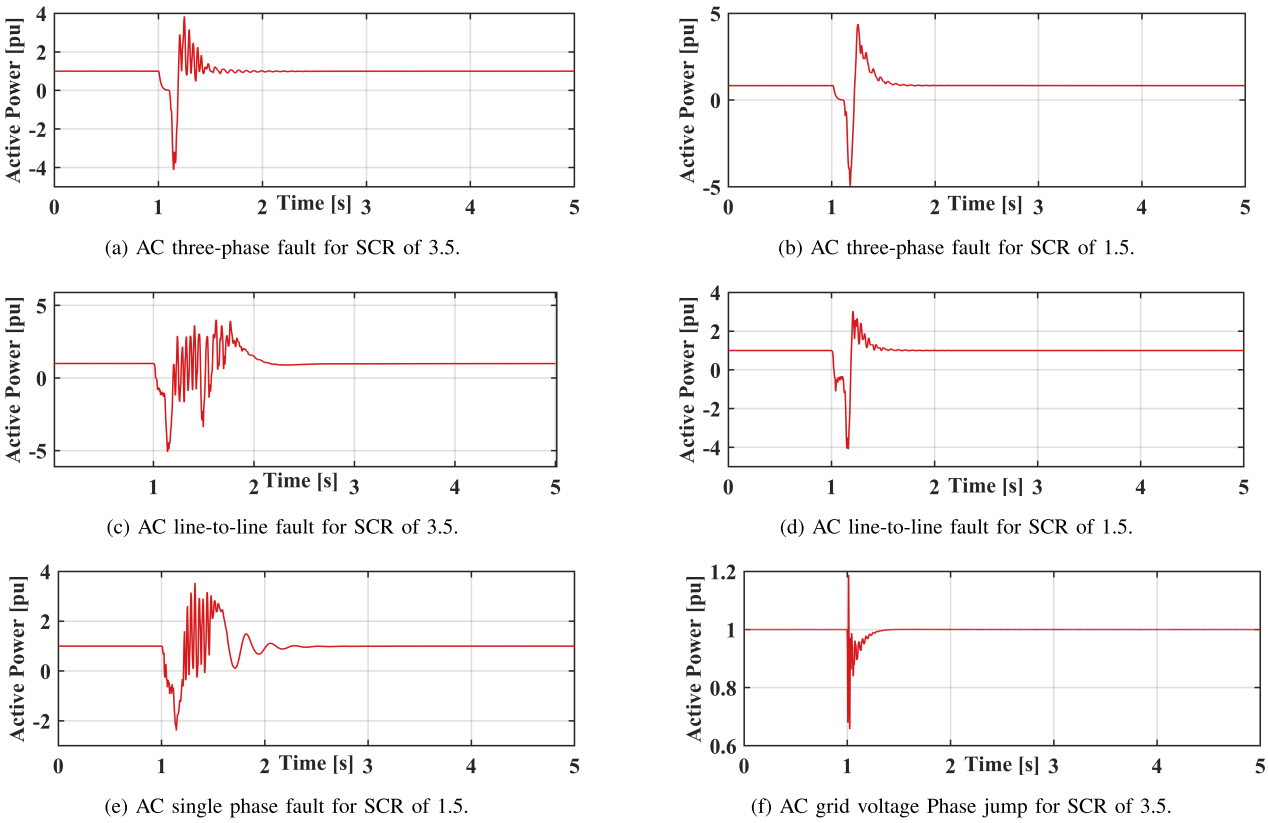

(a) AC three-phase fault for SCR of 3.5.

(b) AC three-phase fault for SCR of 1.5.

(c) AC line-to-line fault for SCR of 3.5.

(d) AC line-to-line fault for SCR of 1.5.

(e) AC single phase fault for SCR of 1.5.

(f) AC grid voltage Phase jump for SCR of 3.5.

FIGURE 15. Active power during various transient phenomena.

stations and the control strategies, along with the trajectories of the dq current errors. This provides better insight into the overall system performance. Fig. 14c shows the dq-current curves during the HCS action for the fault. Fig. 15c shows that the oscillations in the active power curve are dampened after the transient event during HCS action.

Fig. 11 shows the trajectory of the curves for an SCR of 1.5, where GFM works better than GFL during steady state, for a line-to-line fault. For this case, the control strategy employed by the HCS is GFM. In case of a fault, the controller switches between GFM and GFL to take advantage of each control strategy during the transient period. Once the fault is completely cleared and the V_{rms} has reached steady state, the HCS switches to the initial control strategy, the GFM control. Fig. 14d shows the dq-current curves during the HCS action for the fault. Fig. 15d shows that the oscillations in the active power curve are dampened after the transient event during HCS action.

Fig. 12 shows the trajectory of the curves for an SCR of 1.5, where GFM works better than GFL during steady state, and the triggered fault is a single-phase fault. It can be seen that the control strategy employed by the HCS is GFM, and in case of a fault, the controller switches between GFM and GFL to take advantage of each control strategy during the transient period. Due to weak grid conditions, it can be observed that the oscillations in the V_{rms} curve persist for about 1.5 s, even though the switching only occurs for about 0.85 s, implying that oscillations around the 2 s mark are of limited significance to trigger the HCS to switch control strategies. Once the fault is completely cleared and the V_{rms} has reached steady state, the HCS switches to GFM control, which was initially used depending on the SCR. Fig. 14e shows the dq-current curves during the HCS action for the fault. Fig. 15e shows that the oscillations in the active power curve are dampened after the transient event during HCS action.

Fig. 13 shows the trajectory of the curves for an SCR of 3.5, where GFL still operates without having large oscillations, and the occurred transient phenomenon is a phase jump case replicating the anomalous operation of the AC grids connected to the converter stations. It can be seen that the control strategy employed by the HCS GFL, and in case of a fault, the controller switches between GFM and GFL to take advantage of each control strategy during the transient period. Once the fault is completely cleared and the V_{rms} has reached steady state, the HCS switches to GFL control, which is the initial control strategy depending on the SCR. Fig. 14f shows the dq-current curves during the HCS action for the phase jump phenomenon. Fig. 15f shows that the oscillations in the active power curve are dampened after the transient event during HCS action. Figs. 14 and 15, demonstrate that the effect of the HCS on the oscillations in the curves is minimal.

VII. CONCLUSION

This research presents a novel control strategy that dynamically switches between GFL and GFM control strategies to improve the system performance by applying the hyperplanes of the states. With this research, the merits of GFL and GFM control strategies can be harnessed. Furthermore, the presented work demonstrates its effectiveness for the studied HVdc grid simulated in real time, offering a feasible pathway for real-world application. The proposed HCS, which is based on PLFs, is inherently large-signal stable, enabling seamless transitions between the control strategies and thereby improving system robustness and adaptability. Large signal stability during transient events is the primary focus of this article; however, as long as the system remains within the defined polytopic stability region, the HCS is stable for small signal disturbances. The results show that when two control strategies are used with a switching rule, the resulting control strategy behaves as a non-linear control strategy, which is more responsive and faster than its former linear control strategy counterparts. This non-linear control strategy has been further tested for various transient phenomena, and the obtained results confirm that the proposed hybrid switching control strategy not only meets the intended control objectives but also enhances overall system resilience and flexibility compared to single-strategy approaches. However, this PLF derivation holds under the assumption that system parameters remain within defined bounds, or operation under moderately disturbed. The proposed switching strategy also excludes rapid transient switching effects and severe permanent faults that trigger amplitude saturation. Handling such obscure non-linearities and their impact on Lyapunov stability will be covered in future works. While integral wind-up and oscillations from frequency switching were not observed, mitigation strategies(e.g., anti-windup, dwell time, smooth transitions) are acknowledged for future implementation. This work can be applied in offshore HVdc networks and microgrids.

REFERENCES

[1] J. Freytes, "Small-signal stability analysis of modular multilevel converters and application to MMC–based multi-terminal DC grids," Ph.D. dissertation, Ecole Centrale de Lille, Laboratoire d'Électrotechnique et d'Électronique de Puissance, ULR, 2017.

[2] T. Haileselassie and K. Uhlen, "Power system security in a meshed North Sea HVdc grid," *Proc. IEEE*, vol. 101, no. 4, pp. 978–990, Apr. 2013.

[3] A. Korompili, Q. Wu, and H. Zhao, "Review of VSC HVdc connection for offshore wind power integration," *Renew. Sustain. Energy Rev.*, vol. 59, pp. 1405–1414, Jun. 2016.

[4] Q. Taoufik, C. Li, K. Oue, F. Gruson, F. Colas, and X. Guillaud, "Direct AC voltage control for grid-forming inverters," *J. Power Electron.*, vol. 20, no. 1, pp. 198–211, Jan. 2020.

[5] M. G. Dozein, P. Mancarella, T. K. Saha, and R. Yan, "System strength and weak grids: Fundamentals, challenges, and mitigation strategies," in *Proc. Australas. Universities Power Eng. Conf. (AUPEC)*, Nov. 2018, pp. 1–7.

[6] Z. Xu, N. Zhang, Z. Zhang, and Y. Huang, "The definition of power grid strength and its calculation methods for power systems with high proportion nonsynchronous-machine sources," *Energies*, vol. 16, no. 4, p. 1842, Feb. 2023. [Online]. Available: https://www.mdpi.com/1996-1073/16/4/1842

[7] J. Fang, H. Li, Y. Tang, and F. Blaabjerg, "On the inertia of future more-electronics power systems," *IEEE J. Emerg. Sel. Topics Power Electron.*, vol. 7, no. 4, pp. 2130–2146, Dec. 2019. [Online]. Available: https://ieeexplore.ieee.org/document/8506338/

[8] K.-H. Kim, S. Cui, and J.-J. Jung, "Current-oriented phase-locked loop method for robust control of grid-connected converter in extremely weak grid," *IEEE Trans. Power Electron.*, vol. 39, no. 10, pp. 11963–11968, Oct. 2024.

[9] A. Ordono, A. Sanchez-Ruiz, M. Zubiaga, F. J. Asensio, and J. A. Cortajarena, "Current limiting strategies for grid forming inverters under low voltage ride through," *Renew. Sustain. Energy Rev.*, vol. 202, Sep. 2024, Art. no. 114657.

[10] D. Liberzon and A. S. Morse, "Basic problems in stability and design of switched systems," *IEEE Control Systems Mag.*, vol. 19, no. 5, pp. 59–70, Aug. 2002. [Online]. Available: https://ieeexplore.ieee.org/document/793443/

[11] W. Qiu et al., "A grid Forming/Following sequence switching control strategy for supporting frequency stability of isolated power grids," in *Proc. 5th Asia Energy Electr. Eng. Symp. (AEEES)*, Mar. 2023, pp. 212–217. [Online]. Available: https://ieeexplore.ieee.org/document/10114155/

[12] X. Gao, D. Zhou, A. Anvari-Moghaddam, and F. Blaabjerg, "Seamless transitions between grid-following and grid-forming control: A novel switching method," in *Proc. 11th Int. Conf. Power Electron. ECCE Asia (ICPE-ECCE Asia)*, 2023, pp. 1154–1160.

[13] M. Kwon, S. Park, C.-Y. Oh, J. Lee, and S. Choi, "Unified control scheme of grid-connected inverters for autonomous and smooth transfer to stand-alone mode," *IEEE Trans. Power Electron.*, vol. 37, no. 1, pp. 416–425, Jan. 2022.

[14] P. Colaneri and J. C. Geromel, "Parameter-dependent Lyapunov functions for time varying polytopic systems," in *Proc. Amer. Control Conf.*, 2005, pp. 604–608.

[15] A. Lekic, D. Stipanovic, and N. Petrovic, "Controlling the cuk converter using polytopic Lyapunov functions," *IEEE Trans. Circuits Syst. II, Exp. Briefs*, vol. 65, no. 11, pp. 1678–1682, Nov. 2018. [Online]. Available: https://ieeexplore.ieee.org/document/8170285/

[16] A. Lekic, A. E. Aroudi, and D. Stipanovic, "Polytopic control of a PV-fed SEPIC DC–DC converter," in *Proc. IEEE Int. Symp. Circuits Syst. (ISCAS)*, May 2019, pp. 1–5.

[17] I. Masubuchi and Y. Ohta, "Analysis of almost-everywhere stability of a class of discontinuous systems via Lyapunov densities," in *Proc. Eur. Control Conf. (ECC)*, Jun. 2016, pp. 567–574. [Online]. Available: http://ieeexplore.ieee.org/document/7810345/

[18] A. P. Molchanov and Y. S. Pyatnitskiy, "Criteria of asymptotic stability of differential and difference inclusions encountered in control theory," *Syst. Control Lett.*, vol. 13, no. 1, pp. 59–64, Jul. 1989.

[19] R. K. Tarcar et al., "Post DC fault circulating current suppression control," in *Proc. IEEE Power Energy Soc. Gen. Meeting (PESGM)*, Jul. 2023, pp. 1–5.

[20] G. Bergna-Diaz, J. Freytes, X. Guillaud, S. D'Arco, and J. A. Suul, "Generalized voltage-based state-space modeling of modular multilevel converters with constant equilibrium in steady state," *IEEE J. Emerg. Sel. Topics Power Electron.*, vol. 6, no. 2, pp. 707–725, Jun. 2018.

[21] Ö. C. Sakinci, A. Lekić, and J. Beerten, "Generalized impedance-based AC/DC power system modeling for harmonic stability analysis," *Int. J. Electr. Power Energy Syst.*, vol. 143, Dec. 2022, Art. no. 108456.

[22] N. Mohammed, W. Zhou, and B. Bahrani, "Comparison of PLL-based and PLL-less control strategies for grid-following inverters considering time and frequency domain analysis," *IEEE Access*, vol. 10, pp. 80518–80538, 2022.

[23] J. Rocabert, A. Luna, F. Blaabjerg, and P. Rodríguez, "Control of power converters in AC microgrids," *IEEE Trans. Power Electron.*, vol. 27, no. 11, pp. 4734–4749, Nov. 2012.

[24] M. Khan, W. Wu, and L. Li, "Grid-forming control for inverter-based resources in power systems: A review on its operation, system stability, and prospective," *IET Renew. Power Gener.*, vol. 18, no. 6, pp. 887–907, Apr. 2024.

[25] E. Ebinyu, O. Abdel-Rahim, D.-E.-A. Mansour, M. Shoyama, and S. M. Abdelkader, "Grid-forming control: Advancements towards 100% inverter-based grids—A review," *Energies*, vol. 16, no. 22, p. 7579, Nov. 2023. [Online]. Available: https://www.mdpi.com/1996-1073/16/22/7579

[26] Y. Teng, W. Deng, W. Pei, Y. Li, L. Dingv, and H. Ye, "Review on grid-forming converter control methods in high-proportion renewable energy power systems," *Global Energy Interconnection*, vol. 5, no. 3, pp. 328–342, Jun. 2022.
[27] X. Lyu, I. Subotić, and D. Groß, "Unified grid-forming control of PMSG wind turbines for fast frequency response and MPPT," 2022, *arXiv:2207.09536*.
[28] Y. Ohta, "On the construction of piecewise linear Lyapunov functions," in *Proc. 40th IEEE Conf. Decis. Control*, vol. 3, Dec. 2001, pp. 2173–2178. [Online]. Available: https://ieeexplore.ieee.org/document/980577
[29] A. F. Filippov, "Differential equations with discontinuous right-hand side," *Matematicheskii Sbornik*, vol. 93, no. 1, pp. 99–128, 1960.
[30] F. Blanchini, D. Casagrande, and S. Miani, "Modal and transition dwell time computation in switching systems: A set-theoretic approach," *Automatica*, vol. 46, no. 9, pp. 1477–1482, Sep. 2010.
[31] E. Rokrok, T. Qoria, A. Bruyere, B. Francois, and X. Guillaud, "Effect of using PLL-based grid-forming control on active power dynamics under various SCR," in *Proc. IECON 45th Annu. Conf. IEEE Ind. Electron. Soc.*, vol. 1, Oct. 2019, pp. 4799–4804.
[32] Y. He, W. Xiang, P. Meng, and J. Wen, "Investigation on grid-following and grid-forming control schemes of cascaded hybrid converter for wind power integrated with weak grids," *Int. J. Electr. Power Energy Syst.*, vol. 155, Jan. 2024, Art. no. 109524. [Online]. Available: https://www.sciencedirect.com/science/article/pii/S0142061523005811

ROHAN KAMAT TARCAR (Graduate Student Member, IEEE) received the M.Sc. degree in electrical power engineering from Delft University of Technology (TU Delft), The Netherlands, in 2023, where he is currently pursuing the Ph.D. degree. His research interests include real-time transient stability analysis, advanced HVdc control strategies, hybrid control schemes, Lyapunov-based stability methods, and the design and operation of multi-terminal HVdc (MTDC) networks for future power systems.

MARJAN POPOV (Fellow, IEEE) received the Ph.D. degree in electrical power engineering from Delft University of Technology, Delft, The Netherlands, in 2002. He is also a Chevening Alumnus, and in 1997, he was an Academic Visitor with the University of Liverpool, Liverpool, U.K., working in the Arc Research Group on modeling SF6 circuit breakers. His research interests include large-scale power system transients, intelligent protection for future power systems, and wide-area monitoring and protection. He is a member of Cigre and actively participated in WG C4.502 and WG A2/C4.39. In 2010, he received the prestigious Dutch Hidde Nijland Prize for extraordinary research achievements. He was a recipient of the IEEE PES Paper Award and the IEEE Switchgear Committee Award in 2011. He is an Associate Editor of *International Journal of Electrical Power and Energy Systems* (Elsevier) and the Co-Editor-in-Chief of *e-Prime-Advances in Electrical Engineering, Electronics and Energy*.

ALEKSANDRA LEKIĆ (Senior Member, IEEE) received the B.S., M.S., and Ph.D. degrees in electrical engineering from the School of Electrical Engineering, University of Belgrade, Belgrade, Serbia, in 2012, 2013, and 2017, respectively. She was an Assistant Professor from January 2020 to April 2025, and she has been an Associate Professor, since May 2025. She is currently with the Faculty of Electrical Engineering, Mathematics and Computer Science, TU Delft. She leads the Control of the HVdc/AC Power Systems Team, which conducts advanced research in the field of power electronics and power system control. She was a recipient of the prestigious NWO Veni 2022 grant in The Netherlands. She is an Associate Editor of the *International Journal of Electrical Power and Energy Systems* (Elsevier).